Available online at www.sciencedirect.com

jmr&t Journal of Materials Research and Technology

www.jmrt.com.br

Original Article

Microstructure evolution and mechanical properties of X12CrMoWVNbN10-1-1 steel during quenching and tempering process

*Xingang Tao, Chuanwei Li, Lizhan Han, Jianfeng Gu**

Shanghai Key Laboratory of Materials Laser Processing and Modification, School of Materials Science and Engineering, Shanghai Jiao Tong University, Shanghai, China

ARTICLE INFO

Article history:
Received 25 November 2014
Accepted 9 June 2015
Available online 21 July 2015

Keywords:
Microstructure evolution
Mechanical property
X12CrMoWVNbN10-1-1 steel
Heat treatment

ABSTRACT

The effect of heat treatments was investigated on the microstructure evolution and mechanical properties of X12CrMoWVNbN10-1-1 steel. The as-received steel was austenitized at 1080 °C for 16 h and cooled in furnace, following tempered in two steps, i.e. at 570 °C for 18 h and then at 690 °C for 24 h. The austenitized sample had a typical lath martensite structure with some retained austenite and no delta ferrite was observed after austenitization. After the first tempering at 570 °C, there was no retained austenite remained but it resulted in the forming of precipitates, such as Cr-rich M_7C_3, Cr-rich $M_{23}C_6$, Cr-rich M_2N, Nb-rich MN, and the subgrain, as well as the reduction in dislocation density. However, microstructure observation after secondary tempering proved the further arrangement of dislocation, subgrain growth and the coarsening of precipitates. Hardness and impact tests were carried out for establishing a correlation between microstructure and mechanical properties. Finally, a careful fractographic analysis of impact samples had been done using SEM and EDS.

1. Introduction

There are considerable efficiency and environmental advantages to be gained by increasing the steam temperature and pressure, respectively, in fossil power plants. However, severe service condition (high temperature, stress, corrosion, irradiation, etc.) requires the steels to possess excellent comprehensive mechanical properties. Moreover, these steels require a long duration of service, at least more than 30 years [1]. 9–12% Cr ferritic steels have an excellent combination of mechanical properties [2–5]. Their adequate high temperature properties are related to their unique microstructure. The microstructure evolution during heat treatment, such as secondary phase, dislocations and subgrains, directly determines the creep strength of the steels. Commonly, the steels are deformed (forging and rolling) and heat treated (called preheating treatment or after-forging heat treatment) after casting. Then the typical heat treatment (also called quality heat treatment) sequence for high Cr ferritic heat resistant steels includes austenitization to form the austenitic structure and fully or partially dissolve carbonitrides, cooling or

* *Corresponding author.*
E-mail: gujf@sjtu.edu.cn (J. Gu).

http://dx.doi.org/10.1016/j.jmrt.2015.06.001

Table 1 – Chemical composition of the steel.

C	Si	Mn	P	S	Cr	Mo	Ni	W	V	Al	N	Nb
0.11	0.08	0.41	0.008	0.004	10.35	1.00	0.80	1.03	0.18	0.02	0.051	0.040

quenching to transform the austenite to martensite followed by tempering of the martensite structure to improve toughness and ductility. The final microstructure of the steels typically consists of tempered martensite, undissolved and/or re-precipitated carbonitrides [6].

The austenitizing temperature employed during heat treatment determines the partitioning of carbon or nitrogen and alloying elements between the austenite and carbonitrides, with an increase in temperature leading to increased carbonitrides dissolution, higher dissolved alloy element contents and grain growth [7–9]. Once the steels have been austenitized, cooling to below the martensite transformation range facilitates the formation of martensite. In its as-quenched martensitic condition, the steels are hard and brittle and may contain pockets of retained austenite. Quenching is therefore followed by tempering to reduce brittleness, increase ductility and toughness, and reduce residual stress [10]. All the parameters involving in a particular heat treatment process like the austenitization temperature, holding time, the quench medium, cooling rate, tempering temperature and its time affect the final microstructure of the steels. The microstructure in turn controls all the properties that the steels exhibit. The preceding discussion emphasizes the importance of heat treatment in developing the satisfied properties in high Cr ferritic heat resistant steels. Well-defined heat treatment guidelines are therefore required to assist the manufacturer in performing the correct hardening heat treatments to develop optimal properties. Moreover, the microstructure evolution and its relationship with mechanical properties during the heat treatment are not clearly understood. Thus, it is particular interest to study the evolution in the microstructure of the steels during heat treatment so that a better understanding for controlling the microstructure can be obtained to ascertain the safe use for long-term service.

The aim of the present work was to investigate the effect of heat treatments on the microstructure evolution and mechanical properties of X12CrMoWVNbN10-1-1 steel during heat treatment. Microstructure characterization and microchemistry analysis of the precipitates were done using various methods. The relationship between the microstructural evolution and the mechanical properties was also revealed.

Table 2 – Heat treatment parameters.

Symbol of process	Detail heat treatment parameters
A	1080 °C/16 h, furnace cooling
B	570 °C/18 h, air cooling
C	690 °C/24 h, air cooling

Table 3 – Heat treatment process.

Orders of process	Heat treatment process
1	A + B
2	A + B + C

2. Experimental

2.1. Material and heat treatment procedures

The chemical composition of X12CrMoWVNbN10-1-1 steel is given in Table 1. The steel was received in the after-forging heat treatment condition. The initial microstructure of the as-received steel consisted of ferrite with dispersive distributed carbonitrides (Fig. 1). The carbonitrides present in the as-received microstructure were mainly Cr-rich $M_{23}C_6$ and a small amount of Nb-rich MN and Cr-rich M_2N [9]. The heat treatments were performed in an electric resistance furnace. The parameters of heat treatment determined by the finite element method (FEM) simulation [11] are presented in Table 2. The two processes are employed as shown in Table 3.

2.2. Microstructural characterization

The microstructural characteristics of the heat treated specimens were examined with an optical microscope (OM), scanning electron microscope (SEM) and transmission electron microscope (TEM). The samples were ground and

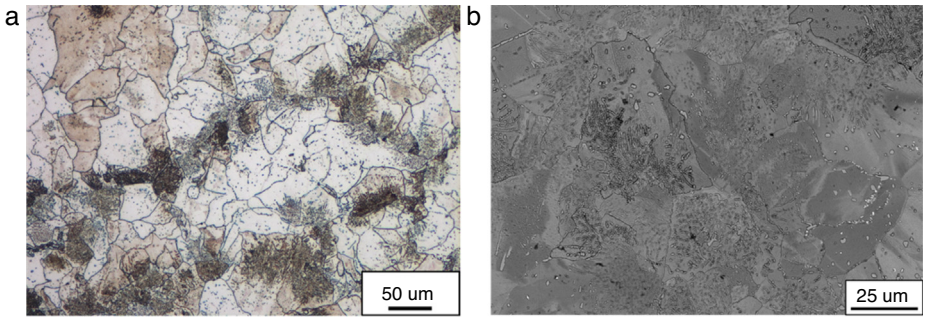

Fig. 1 – OM (a) and SEM (b) micrographs of the steel in as-received state.

polished in the standard manner. The polished samples were etched with a mixture of 10 g iron trichloride, 15 mL hydrochloric acid and 50 mL ethanol for 10 s. The method for displaying the prior austenite grain is in Ref. [9]. The linear intercept method [12] in optical micrographs was employed to estimate the average austenite grain size. For TEM study, thin foils for matrix microstructure observation were prepared in a twin-jet electropolisher, operated at 50 V, in a solution consisting of 95% acetic acid and 5% perchloric acid. The electrolyte temperature was maintained below −30 °C. Conventional TEM observations and energy dispersive spectrometry (EDS) analyses were performed on a JEM-2100 instrument at operating voltage of 200 kV. Fracture surfaces of the impact specimens were examined by scanning electron microscopy to determine the type and mode of fracture.

2.3. Measurements of retained austenite

The volume fraction of the retained austenite present in microstructure was measured by means of magnetization and X-ray diffraction (XRD) measurements. The magnetization measurements were performed in a Physical Property Measurement System (PPMS-9T (EC-II)). The samples were machined to cubes with a size of 2 mm after different heat treatments. The applied magnetic field was changed from 5 to 0 T in steps of 0.25 T at room temperature. Then the volume fraction of retained austenite, f_γ, is determined by a comparison of saturation magnetization (M_s) values in the tested sample, $M_s(c)$, and in the austenite-free sample $M_s(f)$, which method was proposed by Zhao et al. [13],

$$f_\gamma = 1 - \beta\frac{M_s(c)}{M_s(f)} \quad (1)$$

where β is the ratio between the saturation magnetization of the austenite-free sample and that of ferrite, and is calculated to be 0.993 based on the chemical composition of the material. $M_s(c)$ and $M_s(f)$ are determined by the fitting curve of the tested magnetic curve. The sample was tempered twice (570 + 690 °C) after austenitization to obtain the austenite-free specimen as reference, which was checked by XRD. XRD experiments were also carried out using Cu-Kα radiation in a D/max 2550X-ray diffraction analyzer at 35 kV and 200 mA with monochromator. All the measurements were carried out in step scan mode with a scanning speed (2θ) of 3°/min and angular interval 30–110°. The integrated intensities of $(1\,1\,1)_\gamma$, $(1\,1\,0)_\alpha$, $(2\,0\,0)_\gamma$, $(2\,0\,0)_\alpha$, $(3\,1\,1)_\gamma$ and $(2\,1\,1)_\alpha$ peaks were used in the direct comparison method to evaluate the volume fraction of retained austenite [14].

2.4. Characterization of extracted residues

The phase analyses of the precipitates were done on the extracted residues obtained by dissolving the martensite matrix in the electrolyte consisting of 5% glycerol, 1% citric acid monohydrate, 5% hydrochloric acid and methanol in volume fraction. The electric current was 0.7 A and the temperature was between −5 °C and 0 °C. The residues were collected through microporous membrane, washed in distilled water and dried. Their structure was identified by X-ray diffraction (XRD), performed on a D/max 2550X-ray diffraction analyzer at 35 kV and 200 mA. Cu Kα radiation was used and a 2θ range from 20° to 120° was step-scanned with a scanning speed (2θ) of 3°/min. The procedures for analyzing the constituent elements in the extracted residues were Ref. [9].

2.5. Mechanical tests

All mechanical tests were carried out at a room temperature. Determinations of Vickers hardness were made using a 10 kg load on all the heat-treated samples. The load was applied for 15 s. Average of five hardness tests for each testing condition was reported here. Impact tests were conducted on regular size Charpy V-notch specimens (10 mm × 10 mm × 55 mm) on pendulum-type impact testing machine using 300 J hammer. Average of three impact tests for each testing condition was reported here.

3. Results and discussion

3.1. Microstructure observation

3.1.1. Microstructure after austenitization

The prior austenite grain microstructure obtained by austenitized at 1080 °C for 16 h is shown in Fig. 2a. The average diameter of the austenite grain size was approximately 178 μm. The representative microstructure of sample A is shown in Fig. 2b. It is worthy to note that no delta ferrite was observed. Wang [15] had reported that the precipitation of delta ferrite, which is detrimental to the mechanical properties of the material, occurs in X12CrMoWVNbN10-1-1 steel

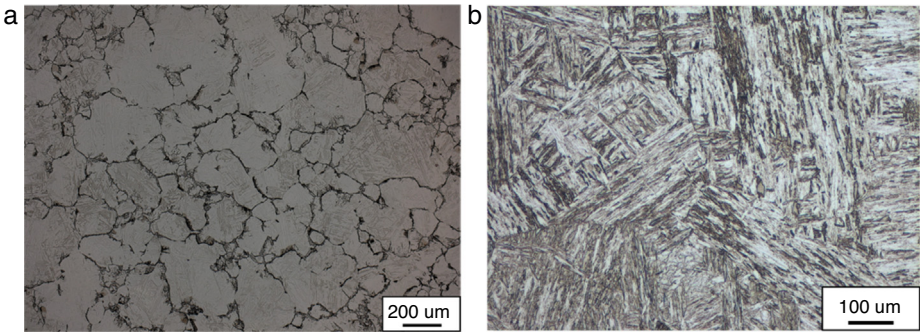

Fig. 2 – Optical micrographs showing prior austenite grain size (a) and microstructure (b) of the sample A.

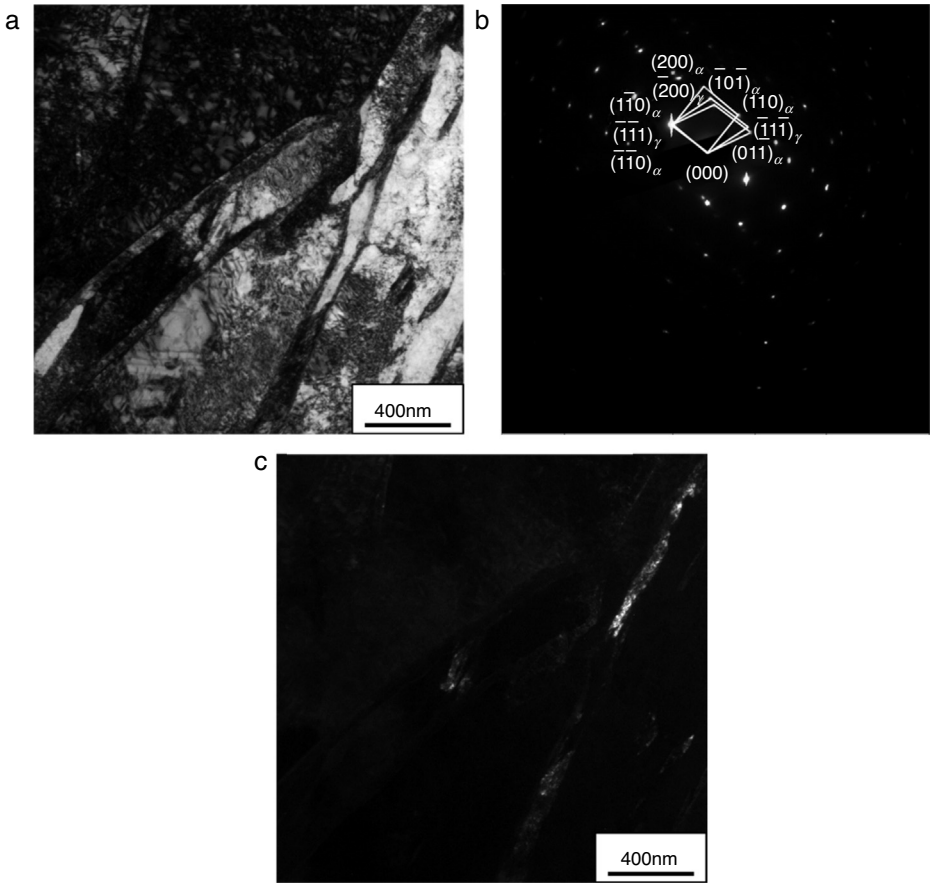

Fig. 3 – TEM micrographs showing typical microstructure of martensite obtained by treatment A; (a) bright-field image; (b) SAED pattern; (c) dark-field image of retained austenite with $(\bar{1}1\bar{1})_\gamma$ reflection.

when the temperature is above 1100 °C and the amount of delta ferrite increases with the austenitization temperature. Cooling in furnace is sufficient to initiate the martensitic transformation after austenitizing treatment due to the high chromium content. The martensite laths contained dense tangled dislocations (Fig. 3a), which was produced by martensite phase transformation during cooling, together with occasional undissolved particles of Nb-rich MN and Fe-rich M_3C by XRD (Fig. 4) and also demonstrated by TEM as shown in Figs. 5 and 6. This confirmed that the extensive carbonitride dissolution occurred during austenitization at 1080 °C for 16 h, but 1080 °C was still below the complete carbonitrides dissolution temperature. These Nb-rich MN particles were very stable at high temperature. It was reported that in this steel more than half of these precipitates were not dissolved after austenitization at 1080 °C for 16 h [16]. These dispersed particles exerted a strong pinning force on the growth of austenite grains [9]. In addition to these Nb-rich MN particles, the microstructure of the specimen A also exhibited the need-like Fe-rich M_3C precipitates. Thin continuous films of retained austenite were observed along lath boundaries, as shown to a light part in the dark-field image in Fig. 3c. The volume fraction of retained austenite determined by X-ray diffraction method [17] and magnetization. Fig. 7 is the magnetic curves for the four different samples by combining the fitting curves with original data. The curves of sample 2 and sample 1 overlapped closely with each other, indicating that there was no retained austenite in sample 1. XRD and magnetization results of the volume fraction of retained austenite measured are given in Table 4, suggesting that the results measured by these two methods were in good agreement.

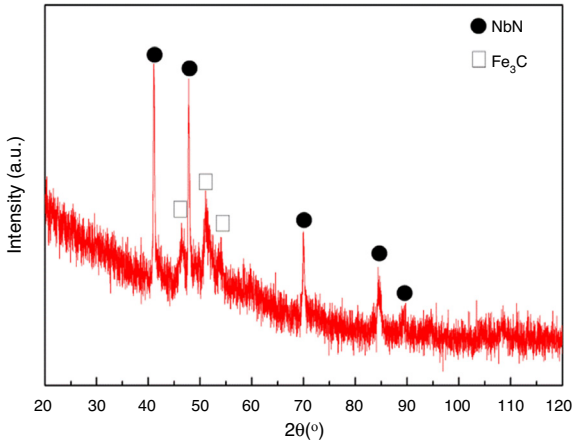

Fig. 4 – XRD pattern of electrolytically extracted precipitates in sample A.

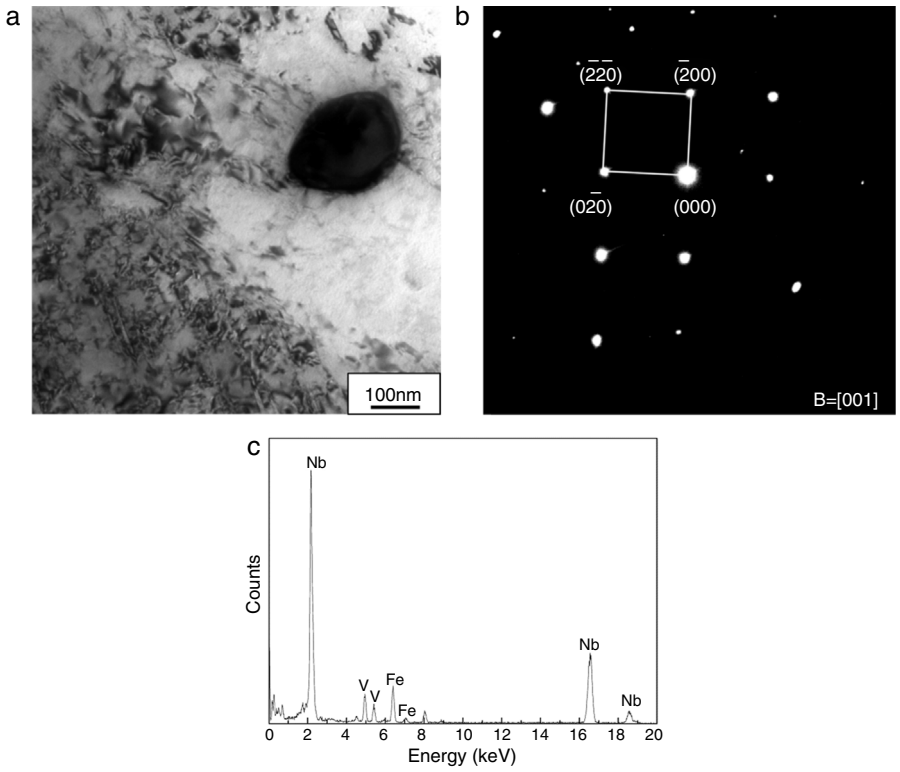

Fig. 5 – TEM analyses of Nb-rich MN particle in sample A: (a) BF micrograph; (b) and (c) are the SAED pattern and EDS spectrum of a Nb-rich MN particle.

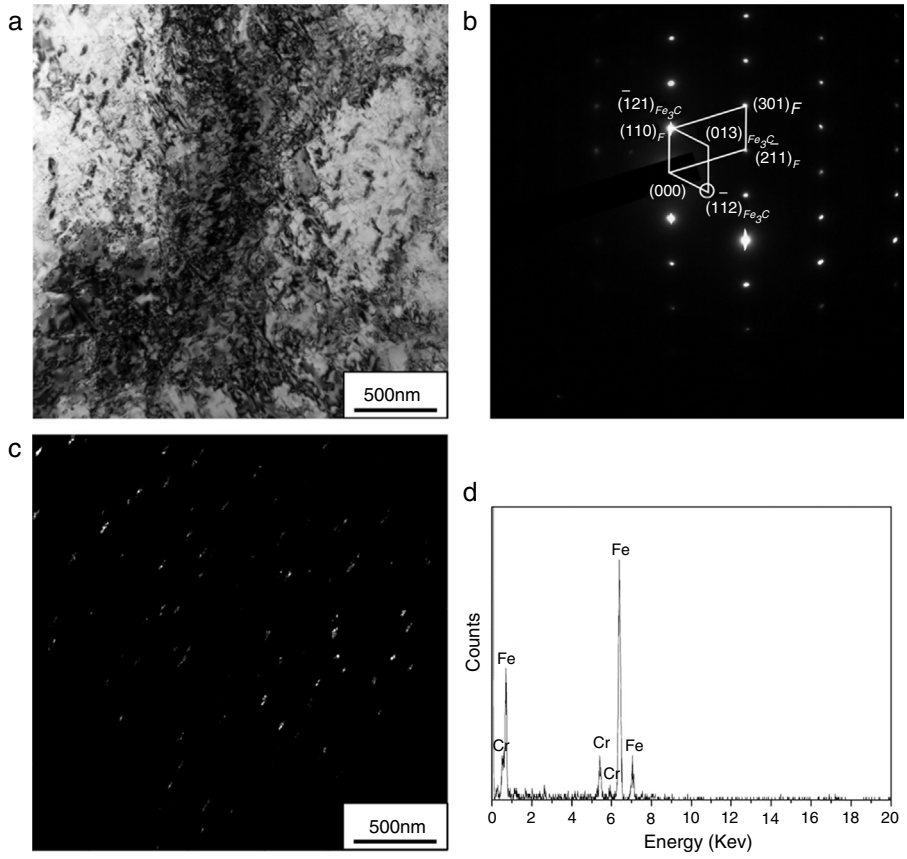

Fig. 6 – TEM analyses of Fe-rich M_3C particles in sample A: (a) BF micrograph; (b) SAED pattern; (c) dark-field (DF) micrograph with $g = (1\bar{1}2)_{Fe_3C}$ reflection and (d) EDS spectrum of a Fe-rich M_3C particle.

Table 4 – The volume fraction of retained austenite measured by XRD and magnetization methods.

Process	XRD measurement (%)	Magnetization measurement (%)
A	9	9.8
1	0	0
2	0	0

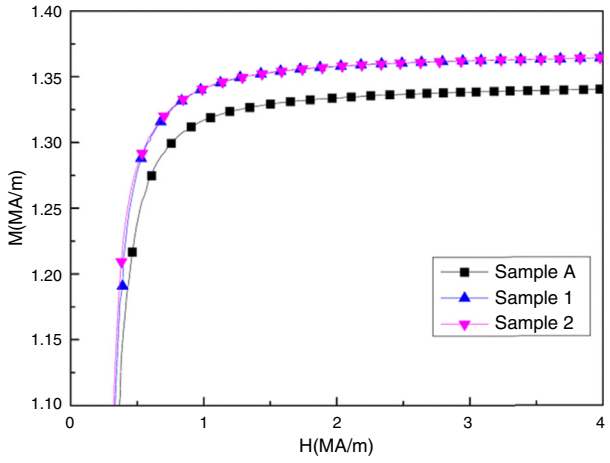

Fig. 7 – The volume fraction of retained austenite measured by magnetization. The pink triangle represents the sample 2, which is austenite-free.

3.1.2. *Microstructure after tempering*

Significant small-scale changes during tempering process were detected by means of SEM and TEM analyses. Subsequent to austenitization, the tempering at lower temperature (570 °C) resulted in profuse precipitation of secondary phases, both on grain boundaries and inside the martensite laths (Fig. 8a) and they were identified as Nb-rich MN, Cr-rich M_7C_3, Cr-rich M_2N and Cr-rich $M_{23}C_6$ by XRD (Fig. 9) and TEM observation Figs. 10–13. A long tempering time of 18 h had resulted in precipitates coarsening at select locations. In sample 1, the Fe-rich M_3C precipitates dissolved as the more stable carbides Cr-rich M_7C_3 formed. They remained distinctly smaller than the heterogeneous ones due to their lower formation temperature [18]. The peaks of the retained austenite were absent in the samples after the first tempering as shown in Fig. 14, which

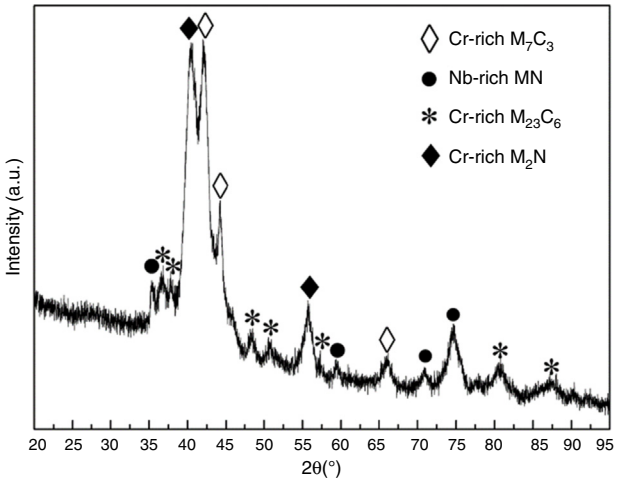

Fig. 9 – XRD pattern of electrolytically extracted residues in sample 1.

was consistent with the results measured by magnetization method. Long term tempering allowed dislocations to anneal out and arrange to form sub-boundaries, which was really only a form of subgrain formation (Fig. 15a). This indicated that the subgrain structure had been formed. This process had often been referred to as recovery during tempering. The tempered martensite structure of high Cr steels was not thermally stable [19], and their static recovery started after an incubation period.

A further tempering at 690 °C produced progressive precipitation and coarsening of the Cr-rich $M_{23}C_6$ carbides concurrent with the gradual elimination of Cr-rich M_7C_3 based on XRD measurement (Fig. 16) and SEM observation (Fig. 8b), indicating an apparent instability of Cr-rich M_7C_3 compared to the Cr-rich $M_{23}C_6$. With their coarsening, the subgrain boundaries became unpinned by precipitates and grew into equiaxed area of ferrite arranged along the former martensite laths, often with boundaries composed of clearly defined dislocation arrays. Dislocations in the tempered martensite subgrains presented regular configurations of a recovered state, as shown in Fig. 15b. The dislocation density after tempering had decreased in comparison with that in the normalized condition. However, it should be noted that a high density of dislocations within martensite laths still remained after tempering, as previous papers reported [20].

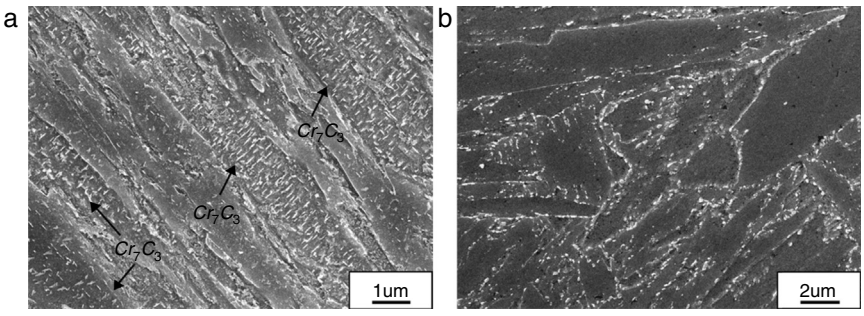

Fig. 8 – SEM micrographs showing the microstructure in samples 1 (a) and 2 (b).

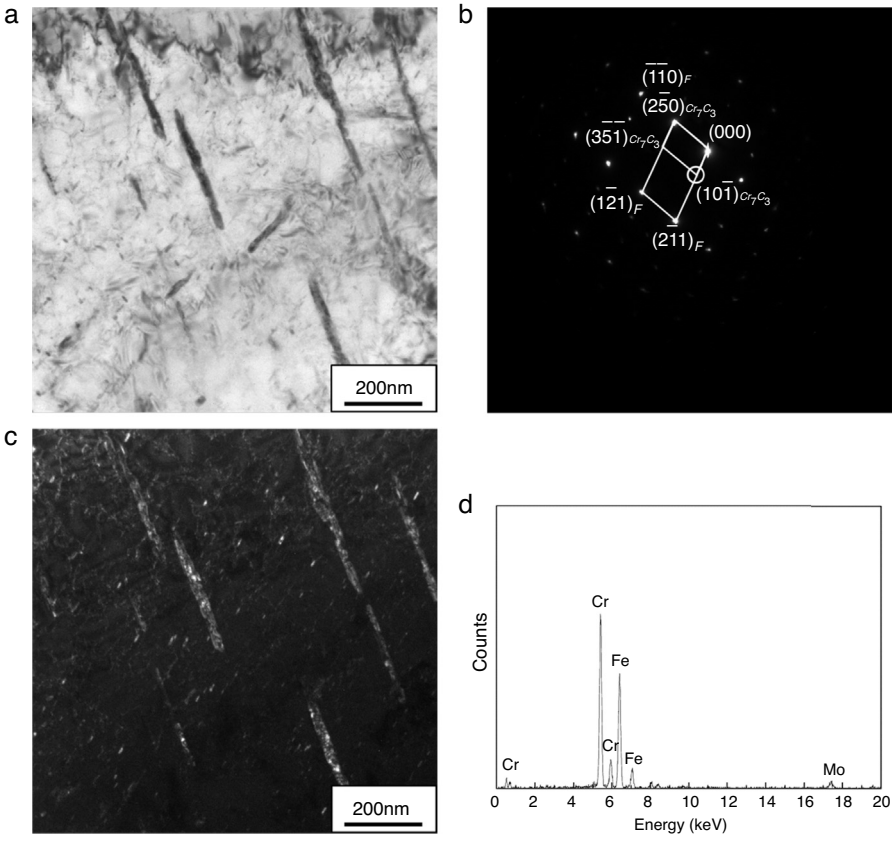

Fig. 10 – TEM analyses of Cr-rich M_7C_3 particles in sample 1: (a) BF micrograph; (b) SAED pattern; (c) DF micrograph with $g = (10\bar{1})_{Cr_7C_3}$ reflection and (d) EDS spectrum of Cr-rich M_7C_3.

3.2. *Microchemistry analyses*

It is acknowledged that the precipitation sequence depends primarily on the relative diffusivities of the alloy elements and the ease of nucleation, the chemistry of the steel is also an important consideration determining which precipitates are favored. The microchemistry experiments of the precipitates extracted from the samples after the heat treatment were carried out and the elements contained in the extracted residue were well established as shown in Table 5.

The concentrations of Nb and N contained in precipitates were almost the same as the given chemistry of the as-received steel, revealing that the matrix was depleted of the solutes Nb and N. However, there was numerous Cr contained in the matrix and only a part (1.408%) existed as a form of precipitate. After austenitization, a part of Nb and enormous quantities of Fe, Cr, W, V, Mo, N were in solution because of the dissolution of precipitates, however, there were still more than half of Nb-rich MN (0.028%) particles existed after austenitization at 1080 °C for 16 h. The detection of Fe and Cr in sample A indicated the precipitation of Fe-rich M_3C carbides resulted from slow cooling. Comparing the microchemical data for samples A and 1, the significant increase in concentration of constituent elements was detected, indicating that the formation of numerous precipitates occurred in the first tempering. The formation of additional Nb-rich MN nitrides was only detected during the first tempering because the concentration of Nb contained in precipitates was 0.04% in sample 1. They precipitated more homogeneously in the martensite laths, probably due to lattice coherence, facilitating nucleation [21]. The increase of the concentrations of Fe and Cr in precipitates from the first tempering to the

Table 5 – The elements contained in extracted residues in steels under different conditions (in wt.%).

States	Fe	Cr	Mo	W	V	Nb	N
As-received	0.519	1.408	0.172	0.224	0.032	0.039	0.051
A	0.274	0.042	0.028	0.04	0.0049	0.028	0.004
1	0.309	1.056	0.195	0.228	0.060	0.039	0.04
2	0.495	1.282	0.188	0.246	0.096	0.039	0.051

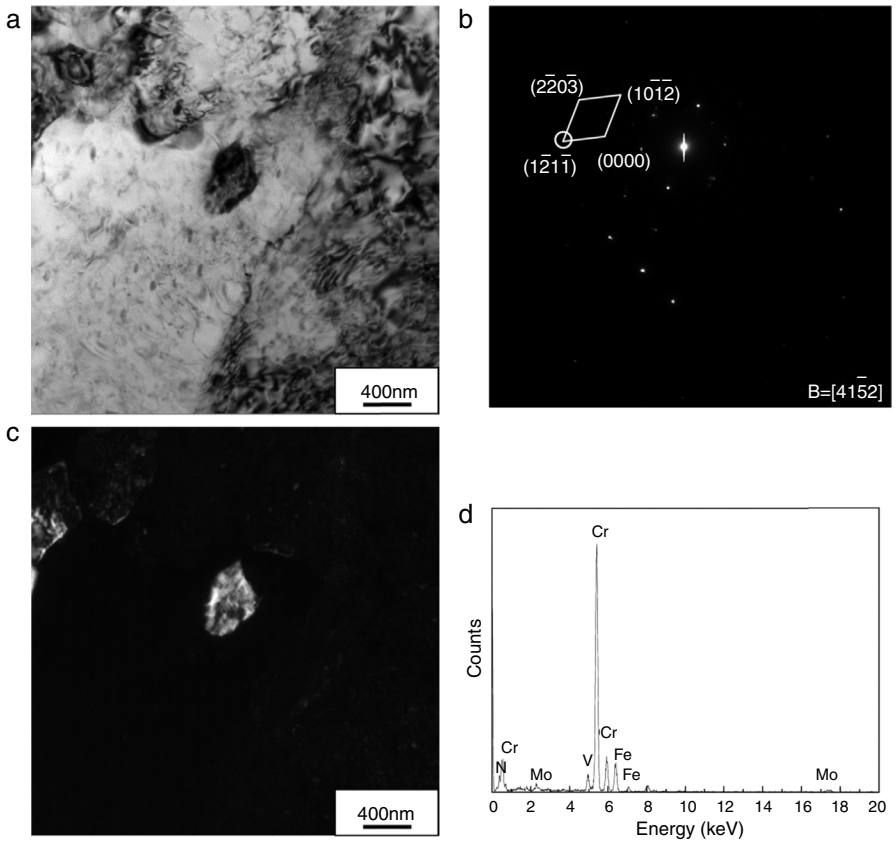

Fig. 11 – TEM analyses of Cr-rich M_2N in sample 1: (a) BF micrograph; (b) SAED pattern; (c) DF micrograph with $g = (1\bar{2}1\bar{1})_{Cr_2N}$ reflection and (d) EDS spectrum of Cr-rich M_2N.

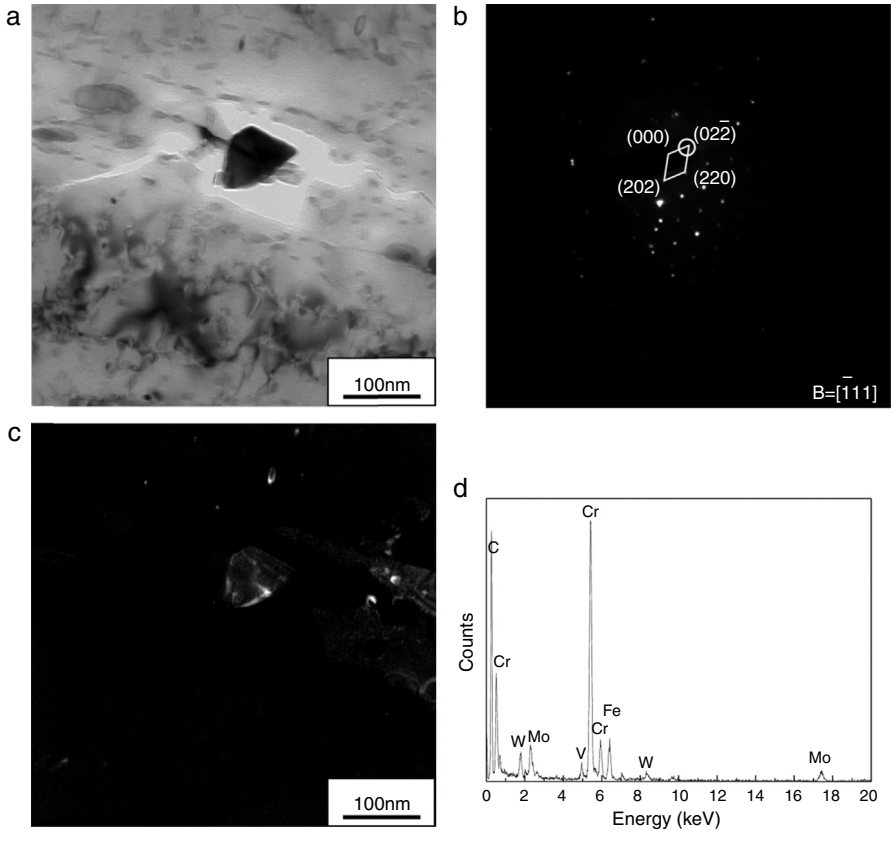

Fig. 12 – TEM analyses of Cr-rich $M_{23}C_6$ in sample 1: (a) BF micrograph; (b) SAED pattern; (c) DF micrograph with $g = (02\bar{2})_{Cr_{23}C_6}$ reflection and (d) EDS spectrum of Cr-rich $M_{23}C_6$.

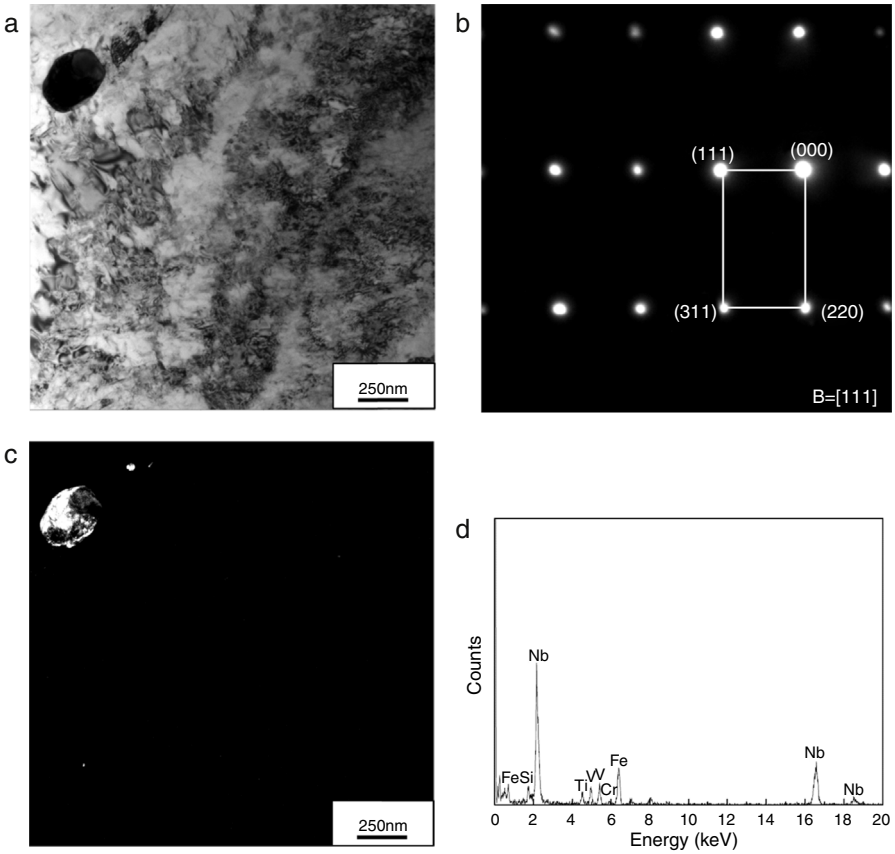

Fig. 13 – TEM analyses of Nb-rich MN particle in sample 1: (a) BF micrograph; (b) and (c) are the SAED pattern and EDS spectrum of a Nb-rich MN particle.

second tempering because the stoichiometric ratio of Cr and Fe to C in Cr-rich $M_{23}C_6$ is larger than that in Cr-rich M_7C_3. Also, the increase of the concentration of N was detected in sample 2 probably caused by the formation of Cr-rich M_2N. Therefore, it was reasonable to consider that the main transformation in the second tempering was the transformation of Cr-rich $M_{23}C_6$ from Cr-rich M_7C_3 and the formation of Cr-rich M_2N.

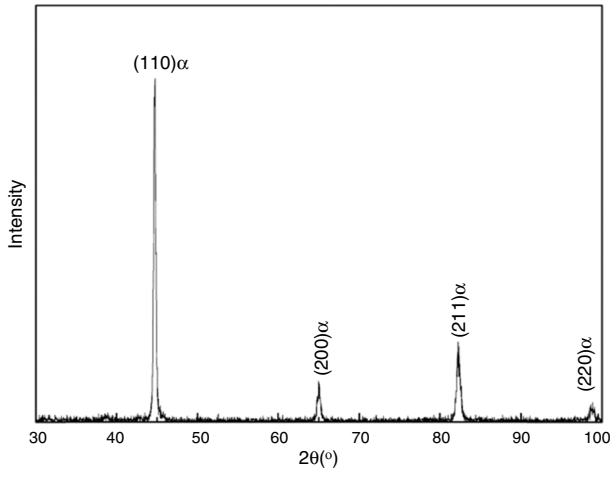

Fig. 14 – XRD patterns of the samples 1 showing that there are no peaks of austenite, only the presence of ferrite reflections are recorded as the carbide volume fraction is rather small.

3.3. *Mechanical properties tests*

Because mechanical properties are influenced by microstructural features, it is important to consider how the microstructures are related to the mechanical properties. Hardness HV_{10}, a reflection of strength, was shown in Fig. 17. The hardness of the sample A was about 430 HV_{10}, compared to 396 HV_{10} of sample 1. The high value of hardness was associated with the solid solution of alloy elements in the matrix resulting from the austenitization of 1080 °C. Compared to the sample 1, a significant drop in hardness was seen after twice tempering. The values of hardness in sample 2 reached 283 HV_{10}. The above mentioned phenomenon could be explained from the following aspects: (1) the diffusion of solid solution strengthening elements, such as Mo and W etc. from matrix into the precipitates took place during tempering due to their formation and coarsening; and (2) the occurring of recovery during tempering involved the annihilation and rearrangement of dislocations, and the growth of subgrain structure [22–26].

Although the decrease of the hardness is always expected, the impact toughness cannot be ignored for this steel; furthermore, it is the prominent in the design. The results of Charpy

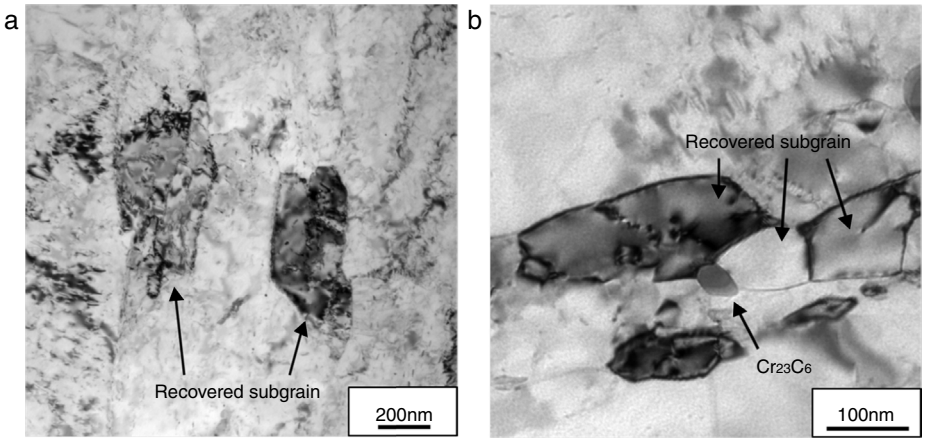

Fig. 15 – TEM micrographs of samples 1 (a) and 2 (b) showing the subgrain microstructure.

impact tests are shown in Fig. 17. In general, the decrease in hardness would be accompanied by an increase in the toughness. After twice tempering (570 + 690 °C), the impact energy of sample 2 reached approximately 33.6 J, higher than that of sample 1 (8.4 J). This phenomenon could be explained by the residual stress caused by martensite transformation from retained austenite and the stress field formed around Cr-rich M_7C_3 particles. Mandziej et al. [27] found that the Cr-rich M_7C_3 carbides formed produced a high stress exerted by them on matrix, which could lead to degradation of the samples. Additionally, through the twice tempering, the variations of the microstructures, including the decomposition of the martensite into polygonal shaped subgrains, contributed effectively to the increase in the impact toughness. There were more interface boundaries in sample 2 due to the formation of subgrains, compared to the sample 1, and these interfaces acted as obstacles for crack propagation, contributing to enhancement of fracture energy. Besides, the increase of the impact energy was partly attributed to the lower Cr content in the matrix due to the precipitation and

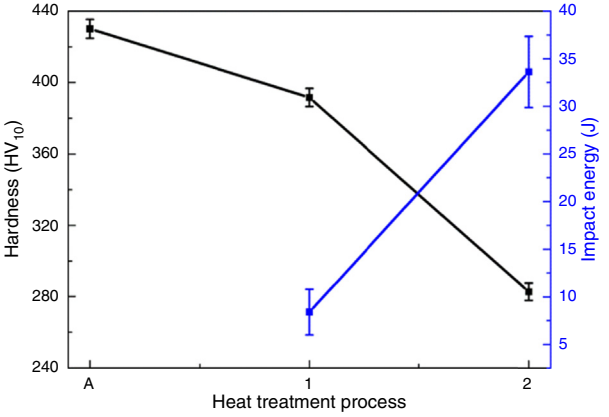

Fig. 17 – Graph showing variation in mechanical properties in response to the heat treatment process.

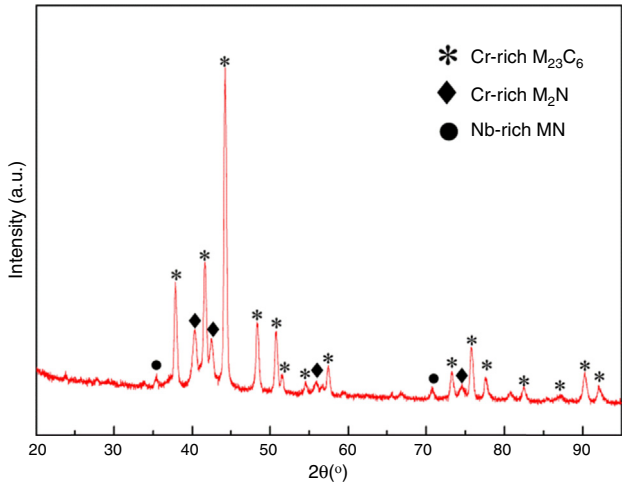

Fig. 16 – XRD pattern of electrolytically extracted residues in sample 2.

growth of Cr-rich carbides. It has been suggested that better fracture toughness correlated with lower Cr content in the alloy [28]. Moreover, the stress exerted by Cr-rich M_7C_3 on the matrix was also released due to the transformation from Cr-rich M_7C_3 into Cr-rich $M_{23}C_6$ during the twice tempering. Finally, the stress caused by the transformation from retained austenite into martensite was also relieved by the secondary tempering.

3.4. *Fracture surfaces observation*

Typical fracture surfaces after Charpy impact test of the heat treated samples were characterized using SEM to evaluate the mode of fracture failure and reveal the nature and morphology of failure. Fig. 18a–c shows the secondary electron images of the typical fracture topography of Charpy specimens. The fracture of sample 1 was flat, without signs of intensive plastic deformation. It was seen from Fig. 18b that the inclusions were isolated and blocky in shape and their sizes vary in range from 10 to 70 μm. Inclusions were found randomly distributed, however, inclusion nests were also observed at some regions. Both

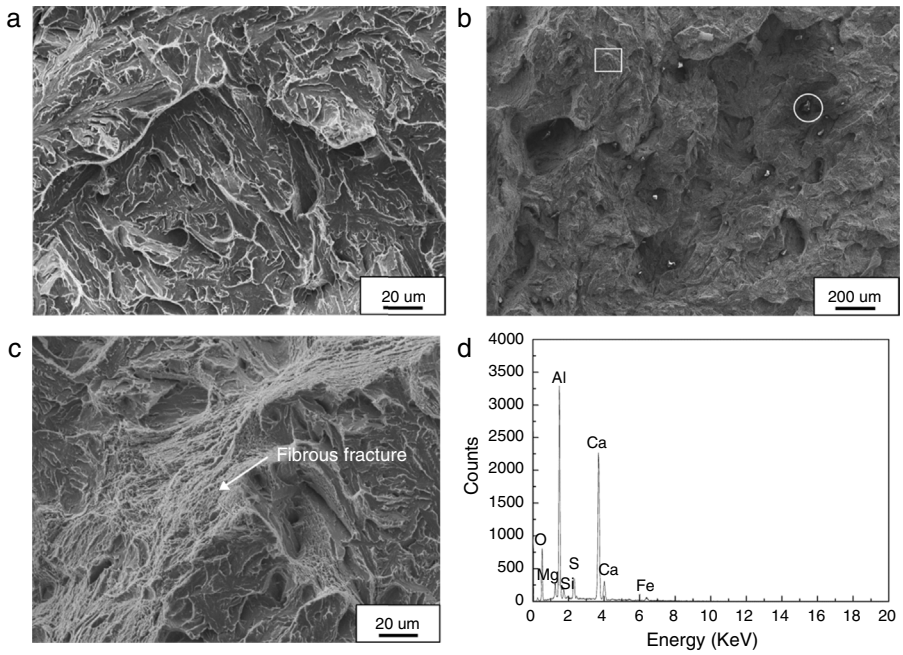

Fig. 18 – SEM micrographs of fracture surfaces of impact samples 1(a), 2(b), (c) is an enlarged view of a box in (b) and (d) EDS spectra of non-metallic inclusion circled in (b).

sulfide and oxide-silicate inclusions were recognized based on EDS spectrum (Fig. 18d). EDS result showed that the inclusions in steel were mostly oxides or sulfides containing mainly Al and Ca with minor Mg, Si and Fe. Generally, every inclusion has its own characteristic shape and appearance [29]. The presence of variety of inclusions and their high density indicated the inadequate cleanliness of the alloy. These inclusions adversely affected the fracture toughness and fatigue strength of the steel [30]. They acted as stress raisers and are potential sites for crack inclusion/matrix interface results in the formation and opening of void. Also, cracks in brittle inclusion or in matrix adjacent to the inclusion were also created [29,31]. Therefore, the fracture of sample 2 was mainly related to the size and dispersive distribution of the inclusion in the steels. However, it was worthy to note that it did not mean that there were no inclusions in sample 1. The matrix was so brittle that the fracture surface followed preferentially the matrix with concentrated stress fields. That's why the inclusions were not observed in the first tempered samples. By comparison, the impact ductility was enhanced by the twice tempering (570 + 690 °C). The cohesion among the matrix was larger than that between the inclusions and the matrix so that cracks were produced between them. That's the reason why there were so many inclusions observed in sample 2. Fig. 18c corresponds to the high magnification SEM fractographs of sample 2. Brittle fracture with quasi-cleavage area was observed, which was a typical fracture in tempered martensitic steels. The main fracture mode was intergranular fracture for the impact samples. The figure documented that cleavage facets size matched prior austenite grain size, or other smaller microstructure subunits, e.g. martensite packet size. Sample 2 also exhibited the brittle fracture with some fibrous fracture consisting of shallow dimples. The shallow dimples indicated that relatively less energy was absorbed by the sample during plastic deformation prior to fracture. Therefore, such fracture morphology was also reflected that the impact energy of sample 2 were higher than that of sample 1.

4. Conclusions

The microstructure evolution and mechanical properties of X12CrMoWVNbN10-1-1 steel during heat treatment were studied. Main conclusions drawn were as follows:

1. Furnace quenching from austenitization at 1080 °C/16 h, the matrix was nearly martensite with small amounts of retained austenite, as well as Fe-rich M_3C and Nb-rich MN particles, and no delta ferrite was detected. Based on the microchemical data, a portion of Nb and enormous quantities of W, V, Mo and N were in solution due to the dissolution of precipitates during austenitization. From the results of XRD and magnetization measurements, the volume fraction of retained austenite after furnace cooling was found to be about 9.4%.
2. Tempering at 570 °C for 18 h initiated the formation of subgrains and allowed disperse precipitates to form. Moreover, no retained austenite remained after first tempering. However, further arrangement of dislocation, subgrain growth into equiaxed area of ferrite and the precipitates coarsening were mainly observed for samples tempered twice at 690 °C for 24 h. In the first tempered state (570 °C), Cr-rich M_7C_3, Cr-rich $M_{23}C_6$, Cr-rich M_2N and Nb-rich MN particles were identified. Following another tempering (690 °C), the

precipitates consisted of Cr-rich M_2N, Cr-rich $M_{23}C_6$ and Nb-rich MN. The precipitation of secondary phases nearly achieved in the first tempering (570 °C). Tempering for 18 h at 570 °C was sufficiently long to achieve the transformation from a part of Cr-rich M_7C_3 into Cr-rich $M_{23}C_6$. The rest of the transformation from Cr-rich M_7C_3 (metastable phase) to Cr-rich $M_{23}C_6$ (stable phase) mainly occurred in the second tempering. Additionally, the formation of Cr-rich M_2N precipitates probably took place at this stage based on the increase of concentration of N.

3. Hardness and impact energy were found significant decreasing/increasing with the treatment going on as expected which was ascribed to a microstructure change with the occurrence of recovery of the martensitic matrix and the formation and growth of precipitates during tempering. And the maximum values of them after the final heat treatment were approximately 283 HV_{10} and 33.6 J, respectively.
4. SEM fractographs of the impact test samples showed primary brittle fracture with quasi-cleavage area. The brittleness of the samples after the first tempering (570 °C) was ascribed to the residual stress caused by martensite transformation from retained austenite and the stress field formed around Cr_7C_3 particles. Besides, the higher Cr content in the matrix was partly attributed to the low impact energy due to the incomplete precipitation of Cr-rich carbides. However, the fracture of the samples after twice tempering (570 + 690 °C) was mainly attributable to the inclusions of sulfide and oxide randomly distributed through the steel, which were detrimental to impact toughness of steel.

Conflicts of interest

The authors declare no conflicts of interest.

Acknowledgements

This work is supported by the National Basic Research Program of China (973Program, Grant No. 2011CB012904), and by CNC machine tools and basic manufacturing equipment technology comments (Grant No. 2012ZX04012011).

REFERENCES

[1] Blaes N, Donth B, Bokelmann D. High chromium steel forgings for steam turbines at elevated temperatures. Energy Mater: Mater Sci Eng Energy Syst 2007;2:207–13.
[2] Bendick W, Ring M. Creep rupture strength of tungsten-alloyed 9–12% Cr steels for piping in power plants. Steel Res 1996;67:382–5.
[3] Haarmann K, Bendick W, Arbab A. The T91/P91 Book. 2nd ed. Vallourec and Mannesmann Tubes; 2002.
[4] Garr K, Rhodes C, Kramer D. Effects of microstructure on swelling and tensile properties of neutron-irradiated Types 316 and 405 stainless steels. ASTM Spec Tech Publ; 1973. p. 109–21.
[5] Klueh R. Heat treatment behavior and tensile properties of Cr–W steels. Metall Trans A 1989;20:463–70.
[6] Di Gianfrancesco A, Cipolla L, Venditti D, Neri S, Calderini M. Creep Behaviour and microstructural analysis of FB2 trial rotor steel'. In: Proc of the Fifth International Conference on Advances in Materials Technology for Fossil Power Plants. ASM International; 2008. p. 366–76.
[7] Caballero F, Alvarez L, Capdevila C, Garcıá de Andrés C. The origin of splitting phenomena in the martensitic transformation of stainless steels. Scr Mater 2003;49:315–20.
[8] Barlow L, Du Toit M. Effect of austenitizing heat treatment on the microstructure and hardness of martensitic stainless steel AISI 420. J Mater Eng Perform 2012;21:1327–36.
[9] Tao XG, Gu JF, Han LZ. Carbonitride dissolution and austenite grain growth in a high Cr ferritic heat-resistant steel. ISIJ Int 2014;54:1704–15.
[10] Hanus R, Schuster F, Buberl A, Cerjak H. Investigations of large turbine casings and valve bodies made of new 9–10% Cr-cast steels and improvement of casting technique and quality performance. In: 6th Liege conference "materials for advanced power engineering". 1998. p. 5–7.
[11] Han LZ. PhD thesis. Shanghai Jiaotong University; 2009.
[12] Vander Voort GF. Metallography, principles and practice. New York: McGraw-Hill Book; 1984.
[13] Zhao L, Van Dijk N, Brück E, Sietsma J, Van der Zwaag S. Magnetic and X-ray diffraction measurements for the determination of retained austenite in TRIP steels. Mater Sci Eng A 2001;313:145–52.
[14] Cullity B, Stock S. Elements of X-ray diffraction. Upper Saddle River, NJ, USA: Prentice Hall; 2001.
[15] Qundi W. The research for the law of δ ferrite precipitated from X12CrMoWVNbN10-1-1 steel. Heavy Cast Forg 2012;6:11–3.
[16] Tao XG, Gu JF, Han LZ. Characterization of precipitates in X12CrMoWVNbN10-1-1 steel during heat treatment. J Nucl Mater 2014.
[17] Miller R. A rapid X-ray method for the determination of retained austenite. Trans ASM 1964;57:892–9.
[18] Abe F, Horiuchi T, Taneike M, Sawada K. Stabilization of martensitic microstructure in advanced 9Cr steel during creep at high temperature. Mater Sci Eng A 2004;378:299–303.
[19] Ghassemi-Armaki H, Chen R, Maruyama K, Yoshizawa M, Igarashi M. Static recovery of tempered lath martensite microstructures during long-term aging in 9–12% Cr heat resistant steels. Mater Lett 2009;63:2423–5.
[20] Zielińska-Lipiec A, Czyrska-Filemonowicz A, Ennis P, Wachter O. The influence of heat treatments on the microstructure of 9% chromium steels containing tungsten. J Mater Process Technol 1997;64:397–405.
[21] Abe F, Taneike M, Sawada K. Alloy design of creep resistant 9Cr steel using a dispersion of nano-sized carbonitrides. Int J Press Vessel Pip 2007;84:3–12.
[22] Little E, Harries D, Pickering F, Keown S. Effects of heat treatment on structure and properties of 12% Cr steels. Met Technol 1977;4:205–17.
[23] Eggeler G. The effect of long-term creep on particle coarsening in tempered martensite ferritic steels. Acta Metall 1989;37:3225–34.
[24] Park I-M, Fujita T, Asakura K. Microstructure and creep rupture properties of a low Si–12 Cr–Mo–V–Nb steel. Trans Iron Steel Inst Jpn 1980;20:99–107.
[25] Abe F, Araki H, Noda T. The effect of tungsten on dislocation recovery and precipitation behavior of low-activation martensitic 9Cr steels. Metall Trans A 1991;22:2225–35.
[26] Ennis P, Czyrska-Filemonowicz A. Recent advances in creep-resistant steels for power plant applications. Sadhana 2003;28:709–30.
[27] Mandziej S, von Rosenstiel A, Goretzki H, Weiss M, Kolster B. Transmission electron microscope and scanning auger

investigations of temper-embrittled 12% Cr steel. Fresenius' Z für Anal Chem 1987;329:335–41.
[28] Andrén H-O, Cai G, Svensson L-E. Microstructure of heat resistant chromium steel weld metals. Appl Surf Sci 1995;87:200–6.
[29] Kiessling R, Lange N. Non-metallic inclusions in steel. Metals Society; 1978.
[30] Böhmer H. A new approach to determine the effect of nonmetallic inclusions on material behavior in rolling contact. ASTM Spec Tech Publ 1993;1195:211–21.
[31] Gigović-Gekić A, Oruč M, Vitez I, Vujičić B. Analyse and research of nonmetallic inclusions for steel 100Cr6. Metalurgija 2009;48:29–32.